A prismatic solid-shell finite element based on a DKT approach with efficient calculation of through the thickness deformation

Hu Xiong, Eduardo Guzman Maldonado, Nahiene Hamila, Philippe Boissé

A prismatic solid-shell finite element based on a DKT approach with efficient calculation of through the thickness deformation

Hu Xiong, Eduardo Guzman Maldonado, Nahiène Hamila, Philippe Boissé*

Université de Lyon, LaMCoS, INSA-Lyon, F-69621, France

In this paper, a prismatic solid-shell is developed. The element is intended to the analysis of shells during forming process and consolidation stage. To correctly perform the simulation of this step, the proposed element provides an accurate calculation of stress/strain through the thickness. The bending stiffness of the element is based on the formulation of a DKT plate element which leads to good numerical efficiency. An additional degree of freedom at the center of the element, allows at the same time, the use of a complete 3D constitutive law, to avoid the thickness locking and a variation of the normal stress in the thickness which makes it possible to check the load boundary conditions on the upper and lower surfaces. This is very important for process simulation, and in particular for consolidation. A set of examples shows the good precision of the proposed element in many of the classical shell tests and its ability to calculate with accuracy the normal strain/stress in thickness.

1. Introduction

Solid-shell elements bridge the gap between shell finite elements and 3D finite elements. Efficient shell elements have been developed based on assumed strain: Dvorkin and Bathe present an assumed method so called 'mixed interpolation' in the case of Ahmad for node shell elements [1], Belytschko et al. propose an assumed strain method to stabilize a 9-node shell element [2], Onate et al. introduced shear constrained plate elements [3], Brank et al. use the assumed strain concept in a shell model accounting for through-the-thickness stretching [4], Katili et al. developed recently a shell element for composite structures using assumed strain fields [5]. Other shell finite elements are based on enhanced assumed strain [6–8], discrete Kirchhoff [9,10], mixed formulations [11, 12] or reduced integration with hourglass control [13–15] (among many).

Many structures have both three-dimensional and thin areas and need in the same finite element analysis, shell and 3D elements. The use of solid-shell elements avoids having two types of element and defining their boundaries and links. The solid-shells are 3D elements, have only degrees of freedom of translation, but have a bending accuracy equivalent to that of the shell elements when the structure is thin. Moreover, the solid-shell elements have other advantages: the effective taking into account of the contact (for example with a tool) directly on the external surfaces and a 3D constitutive law whereas the shell finite elements are generally in a plane stresses state.

Given the 3D kinematics and the 3D constitutive law, it is possible for a solid-shell element to model the strain/stress in the thickness. This possibility can be a major aspect of the analysis performed. For example, consolidation is an important point when forming a thermoplastic prepreg [16,17]. The loads applied to the prepregs during the manufacturing process should lead to a good cohesion of the matrix. Fig. 1 shows a prepreg consisting of ten carbon unidirectional reinforcement plies and thermoplastic matrix [18]. Fig. 1a shows, at the beginning of the process, that the laminate has significant porosities. It is important that the process leads to a state such that Fig. 1b where the matrix is consolidated i.e. with no porosity. In the simulation of the process, the UD (unidirectional) prepreg plies (that are thin) are modeled by elements in contact with the neighboring plies and with the tools. The 3D solid elements cannot be used given the thin thickness of the plies. To model both the forming (and the associated bending) and the compaction/consolidation, solid-shells can be use provided that they correctly model the strain/stress through the thickness.

In addition complex shapes and remeshing during the process lead to use triangular elements in the plane of the structure. This is the objective of this paper: to propose a simple prismatic solid-shell element that is effective in bending and which accurately describes the strain/stress in the thickness.

Much effort have been devoted to the development of solid-shell

* Corresponding author.
E-mail address: Philippe.Boisse@insa-lyon.fr (P. Boisse).

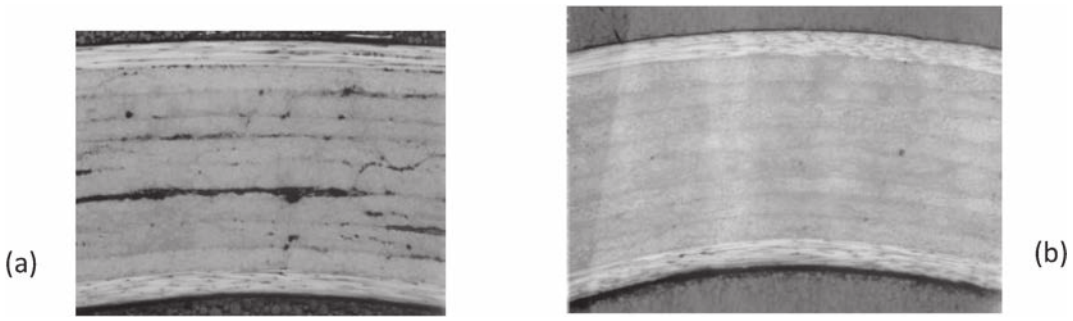

Fig. 1. Prepreg (a) during forming (b) after consolidation.

elements. Most of them are height node elements [19–26]. Hauptmann and Schweizerhof introduced the solid shell concept [19], Vu-Quoc and Tan presented a simple low order hexahedral solid shell element [20], Reese proposed an eight-node solid shell finite element formulation based on reduced integration and hourglass stabilization [21], De Sousa et al. developed a one point quadrature assumed strain 8-node solid shell element [22], Abed-Meraim and Combescure presented a hexahedral solid shell element based on a reduced integration and physical stabilization procedure [23], Schwarze and Reese used EAS and ANS in a reduced integration solid shell element at large deformations [24], Bassa et al., proposed a hexahedral solid-shell with a supplementary node at the center of the element which makes a 3D constitutive law possible [25], Flores presented a 8-node solid-shell element for the analysis of elastic-plastic shells at large strains [26]. Some primes have also been developed [27–29]. Among the first developments Sze and Ghali [30] introduced adjustable parameters in the 8-node hexahedral hybrid element developed by Pian and Tong [31]. Actually, low degree 3D elements are subject to locking phenomena when the thickness is small. Solid-shell element development requires modifications to avoid them. Transverse shear locking is due to the inability of C^0 shell elements to obtain solutions with zero-value transverse shear strains in the case of thin thickness. The thickness locking is due to the coupling between normal and in-plane stresses in the cases of bending. A simple way to avoid thickness locking is to apply a plane stress condition. But the constitutive law is no longer tridimensional.

The reduced integration scheme is the most standard way to avoid locking. In addition this method reduces the computation time which is very interesting in practice. The association of the reduced integration with the methods ANS (assumed natural strain) [1,32] and methods EAS (enhanced assumed strain) [6,33,34] led to the development of efficient solid-shell elements [7,19,21–24,35–37].

The solid-shell finite element proposed in this paper (called SB7γ19: Shell Brick, 7 nodes, 19 degree of freedom) is a 6 node prism i.e. 18 translation degrees of freedom to which a degree of freedom of translation along the thickness at the center of the element is added to improve the through the thickness behavior. The element uses the formulation of the DKT6 shell element for bending [38,39]. This results in a good efficiency in bending. The developed prism belongs to the family of discrete kirchhoff elements. This approach leads to zero transverse shear strains. Nevertheless the transverse shear strains are computed to stabilize zero energy modes that can develop in the prism. An additional dof (displacement along the normal) render possible both to use 3D constitutive laws, to avoid the thickness locking and to verify the boundary conditions in efforts on the upper and lower edges of the element.

A set of standards tests for the shell finite elements shows a good accuracy of the proposed prism. In three of these tests (circular clamped plate, Scordelis-Lo roof, and double dome), the stresses in the thickness are analyzed to check the normal stresses and the respect of the boundary conditions on the outer surfaces of the element.

2. Deformation modes of the prism and approaches considered

The deformation modes of a six node prism are presented in Fig. 2. (The rigid modes are not shown). The presented finite element brings rigidity to these different modes by effective formulations. Bending stiffness (modes 7,8,9) is based on a DKT6 plate finite element [38,39] that brings efficiency in bending (section 3.1 and 3.2).

A standard CST (Constant Strain Triangle) formulation is used for the membrane mode (modes 1,2,3) (section 3.3). In the transverse direction z (modes 4,5,6), a reduced integration and an hourglass control are applied to decrease the computational cost [41] (section 3.5). To improve the transverse behavior a central node is introduced in section 3.5.2. This node renders possible the use of a full three dimensional constitutive law (i.e. without uncoupling). In addition, the pressure boundary conditions on the top and bottom surfaces are verified. The stiffnesses of the DKT formulation leads to zero transverse shear strains. However, the 6-node prism has some zero energy modes with respect to DKT, membrane and pinch stiffnesses. These are stabilized by calculating the transverse shears. The twist mode 10 is not stabilized because it is not propagable.

The principle of virtual work is written,

$$W_{ext}(\mathbf{u},\delta\mathbf{u}) - W_{\text{int}}(\mathbf{u},\delta\mathbf{u}) = W_{acc}(\mathbf{u},\delta\mathbf{u}) \tag{1}$$

for any virtual displacement $\delta\mathbf{u}$ equal to zero on the boundary. $W_{ext}, W_{\text{int}}, W_{acc}$ are the external, internal and inertial virtual works. In the case of the proposed solid-shell element, the internal virtual works is the sum of bending, membrane and pinching:

$$W_{\text{int}}(\mathbf{u},\delta\mathbf{u}) = W_{\text{int}}^{bending}(\mathbf{u},\delta\mathbf{u}) + W_{\text{int}}^{membrane}(\mathbf{u},\delta\mathbf{u}) + W_{\text{int}}^{pinch}(\mathbf{u},\delta\mathbf{u}) \tag{2}$$

In the context of a finite element interpolation, Eqs. (1) and (2) lead to

$$\mathbf{M}\ddot{\mathbf{u}} + \mathbf{F}_{\text{int}}^{bending} + \mathbf{F}_{\text{int}}^{membrane} + \mathbf{F}_{\text{int}}^{pinch} - \mathbf{F}_{\text{ext}} = 0 \tag{3}$$

$\mathbf{M}$ is the masse matrix, $\ddot{\mathbf{u}}$ the nodal acceleration vector and $\mathbf{F}_{\text{ext}}$ is the nodal external load. The interior loads $\mathbf{F}_{\text{int}}^{bending}, \mathbf{F}_{\text{int}}^{membrane}, \mathbf{F}_{\text{int}}^{pinch}$ (bending, membrane, transverse shear and pinching) are the assembly of the element nodal loads $\mathbf{F}_{e,\,\text{int}}^{\alpha}$:

$$\mathbf{F}_{e,\,\text{int}}^{\alpha} = \int_{\Omega_e} \mathbf{B}^{\alpha\mathbf{T}}\boldsymbol{\sigma}^{\alpha} d\Omega \tag{4}$$

where α is the considered mode, α = bending, membrane and pinching. $\boldsymbol{\sigma}^{\alpha}$ is the Cauchy stress corresponding to the deformation mode α. The definition of the strain interpolation matrix $\mathbf{B}^{\alpha}$ for each deformation mode α is the objective of the following section 3.

In the sequel, the displacements and strains considered to determine the strain interpolation matrices are small or virtual. The interpolations of virtual displacement and strains enable geometric nonlinearities using an explicit method. The geometry of the prismatic element is presented Fig. 3.

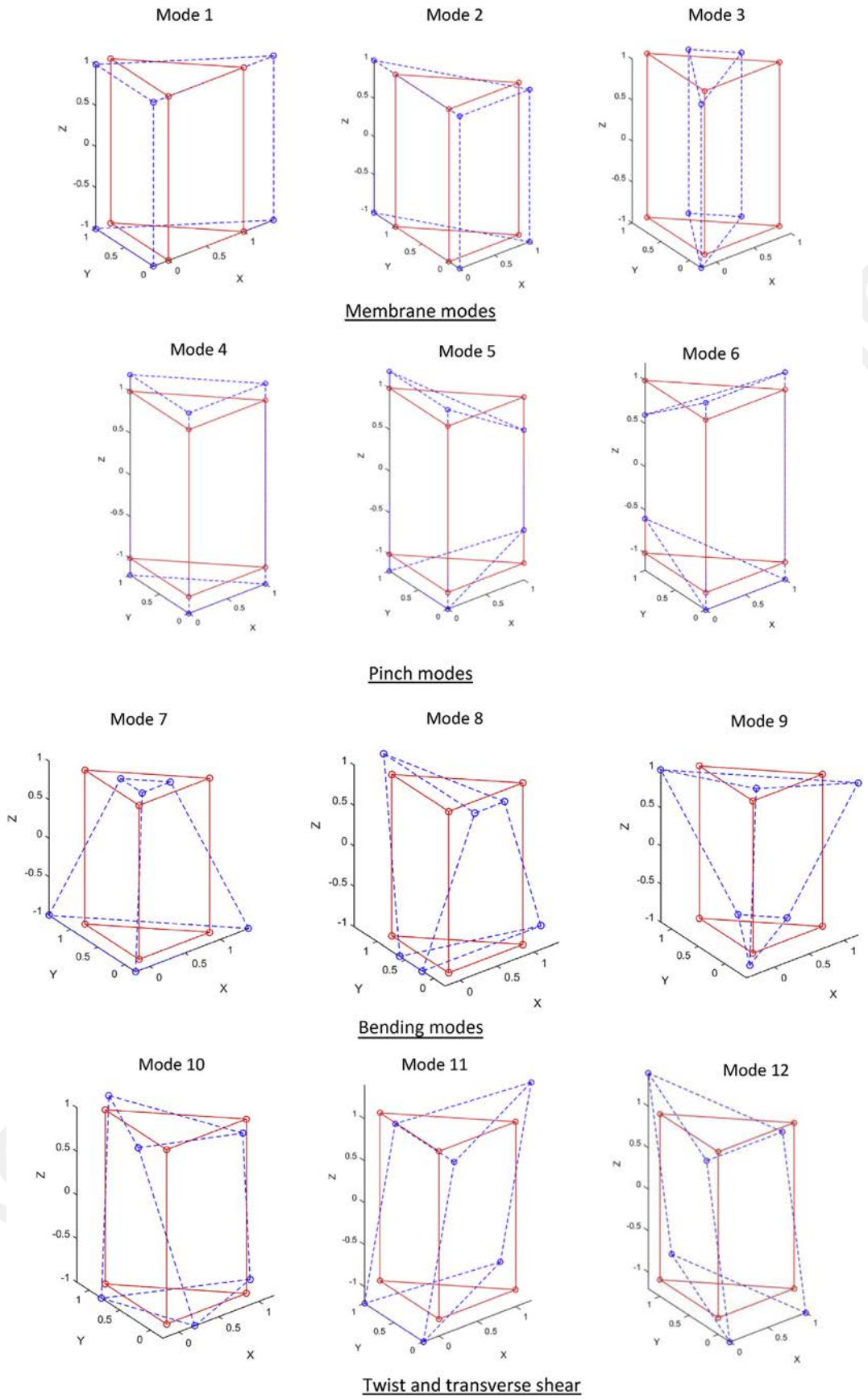

Fig. 2. Deformation modes of the six node prism.

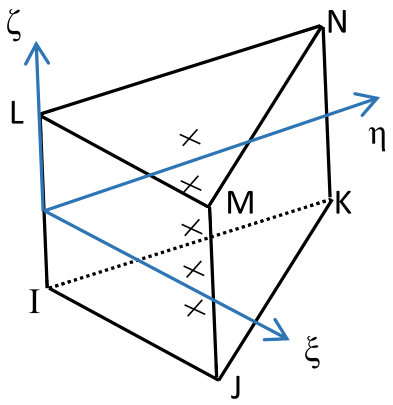

Fig. 3. The prismatic element and the six apex nodes.

3. Strain interpolations of the prismatic element

3.1. Discrete Kirchhoff DKT6 finite element

The bending stiffness corresponding to the bending modes (modes 7, 8, 9 Fig. 2) is based on the kinematics of the discrete Kirchhoff plate element DKT6 [38,39,42]. The stiffness matrix of this element coincides with that of the Morley triangle plate element [43]. The degrees of freedom of the element are three normal displacements at the vertices 1, 2, 3 and three rotations at the middle nodes 4, 5, 6. (Fig. 4). The normal displacement is linearly interplolated:

$$w = N_1 w_1 + N_2 w_2 + N_3 w_3 \tag{5}$$

$$\textit{where} \qquad N_1 = 1 - \xi - \eta \qquad N_2 = \xi \qquad N_3 = \eta \tag{6}$$

ξ, η, ζ are the coordinates in the reference element. The rotations components at the nodes k = 4, 5, 6 located in the middle of the sides are interpolated by:

$$\theta_x = \sum_{k=4,5,6} N_k \theta_{xk} \qquad \theta_y = \sum_{k=4,5,6} N_k \theta_{yk} \tag{7}$$

θ_{xk} and θ_{yk} are the components of the rotation at node k in the Cartesian frame $\mathbf{e}_x$, $\mathbf{e}_y$ in the mid-plane of the element. The interpolation functions N_k are such that:

$$N_4 = 1 - 2N_3 \qquad N_5 = 1 - 2N_1 \qquad N_6 = 1 - 2N_2 \tag{8}$$

Denoting θ_{sk} and θ_{nk} the components of the rotation at node k in the direction of the side k and on the normal perpendicular to the side (Fig. 4a), discrete Kirchhoff assumptions set θ_{nk} in function of the normal displacements (denoted w_i and w_j) of the two ends of the side k of length L_k:

$$\theta_{nk} = \frac{w_i - w_j}{L_k} \tag{9}$$

This reduces the rotation degrees of freedom to the components along the sides $\theta_{s4}, \theta_{s5}, \theta_{s6}$ that are denoted $\theta_4, \theta_5, \theta_6$ for simplicity (Fig. 4).

The curvatures

$$\boldsymbol{\chi} = [\chi_{xx}, \chi_{yy}, \chi_{xy}]^T = \left[-\frac{\partial \theta_x}{\partial x}, -\frac{\partial \theta_y}{\partial y}, -\left(\frac{\partial \theta_y}{\partial x} + \frac{\partial \theta_x}{\partial y}\right) \right]^T \tag{10}$$

are interpolated using Eqs. (6) and (8). The derivatives of the interpolation function N_k are constant. Consequently the curvature is constant on the element. Introducing s_k and c_k the cosine directors on the side k of length L_k,

$$[\boldsymbol{\chi}] = \frac{1}{A} \begin{bmatrix} s_4 L_4 & 0 & s_5 L_5 & 0 & s_6 L_6 & 0 \\ 0 & -c_4 L_4 & 0 & -c_5 L_5 & 0 & -c_6 L_6 \\ -c_4 L_4 & s_4 L_4 & -c_5 L_5 & s_5 L_5 & -c_6 L_6 & s_6 L_6 \end{bmatrix} [\boldsymbol{\theta}_e] \tag{11}$$

where $[\boldsymbol{\theta}_e] = [\theta_{x4}, \theta_{y4}, \theta_{x5}, \theta_{y5}, \theta_{x6}, \theta_{y6}]^T$ and A is the area of the triangle 1,2,3. In the frame of the sides:

$$[\boldsymbol{\chi}] = \frac{1}{A} \begin{bmatrix} \ldots & s_k c_k L_k & \ldots & \ldots & s_k^2 L_k & \ldots \\ & -s_k c_k L_k & & & c_k^2 L_k & \\ & -c_k^2 L_k + s_k^2 L_k & & & -2 s_k c_k L_k & \end{bmatrix} [\boldsymbol{\theta}_s] \tag{12}$$

where $[\boldsymbol{\theta}_s] = [\theta_{n4}, \theta_{n5}, \theta_{n6}, \theta_4, \theta_5, \theta_6]^T$.

The components θ_{nk} are related to the normal displacements w_i by the discrete Kirchhoff conditions (Eq. (9)), the interpolation of the curvatures is in the form:

$$[\boldsymbol{\chi}] = [\mathbf{B}_\theta] \begin{bmatrix} \theta_4 \\ \theta_5 \\ \theta_6 \end{bmatrix} + [\mathbf{B}_w] \begin{bmatrix} w_1 \\ w_2 \\ w_3 \end{bmatrix} \tag{13}$$

with

$$[\mathbf{B}_\theta] = \frac{1}{A} \begin{bmatrix} s_4^2 L_4 & s_5^2 L_5 & s_6^2 L_6 \\ c_4^2 L_4 & c_5^2 L_5 & c_6^2 L_6 \\ -2 c_4 s_4 L_4 & -2 c_5 s_5 L_5 & -2 c_6 s_6 L_6 \end{bmatrix} \tag{14}$$

$$[\mathbf{B}_w] = \frac{1}{A} \begin{bmatrix} c_4 s_4 - c_6 s_6 & c_5 s_5 - c_4 s_4 & c_6 s_6 - c_5 s_5 \\ c_6 s_6 - c_4 s_4 & c_4 s_4 - c_5 s_5 & c_5 s_5 - c_6 s_6 \\ -c_4^2 + s_4^2 + c_6^2 - s_6^2 & -c_5^2 + s_5^2 + c_4^2 - s_4^2 & c_5^2 - s_5^2 - c_6^2 + s_6^2 \end{bmatrix} \tag{15}$$

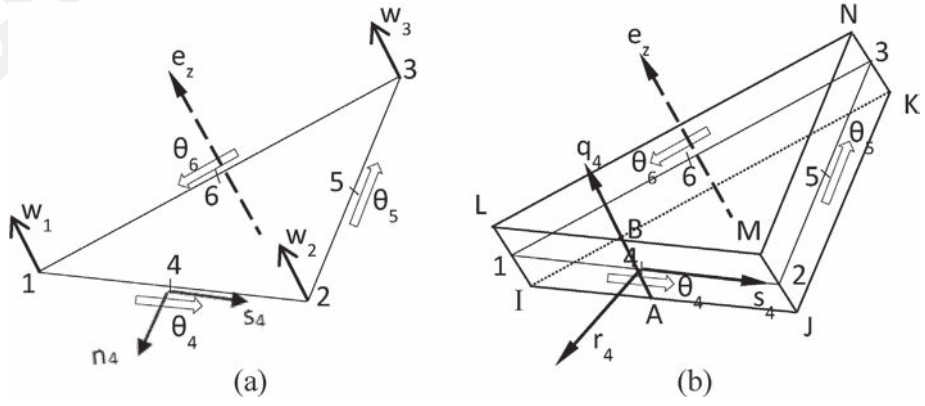

Fig. 4. (a) DKT6 plate finite element, (b) corresponding prismatic element.

3.2. Linking the DKT6 triangle to the prism element

The element proposed in this paper is a prism. For bending, it is based on the DKT6 element described above. But the nodes (I, J, K, L, M, N) are at the vertices of the prism (Fig. 4b). The curvatures (Eq. (13)) must be expressed in function of the displacements of (I, J, K, L, M, N). The normal displacements at the nodes of the DKT6 are directly related to the displacements of the vertice nodes of the prisme

$$w_1 = \frac{w_I + w_L}{2}; \quad w_2 = \frac{w_J + w_M}{2}; \quad w_3 = \frac{w_K + w_N}{2} \tag{16}$$

A base change of $\mathbf{B}_w$ (Eq. (15)) gives $\overline{\mathbf{B}}_w$ that interpolates the part of the curvature function of the normal displacements in function of the 18 nodal displacements of the prism $[\mathbf{U}_e]$.

$$[\mathbf{U}_e] = [U_{XI}, U_{YI}, U_{ZI}, U_{XJ}, U_{YJ} \ldots\ldots U_{ZN}]^T \tag{17}$$

The rotations $\theta_4, \theta_5, \theta_6$ around the three sides of the triangle must be expressed in function of the nodal displacements of the prism $[\mathbf{U}_e]$. Consider node 4. Two points A and B are located in the middle of the edges IJ and LM (Fig. 4b). A local basis is defined at node 4. $\mathbf{s}_4$, $\mathbf{q}_4$ are the unit vectors along 1–2 and A-B respectively. $\mathbf{r}_4$ completes the orthonormal system. The components of $\mathbf{s}_4$, $\mathbf{q}_4$, $\mathbf{r}_4$ in the global system gives the rotation $\mathbf{R}_4$ that connect the displacements and coordinates of the node I in the local (4) and global system.

$$\begin{bmatrix} u_I^{(4)} \\ v_I^{(4)} \\ w_I^{(4)} \end{bmatrix} = [\mathbf{R}_4] \begin{bmatrix} U_{XI} \\ U_{YI} \\ U_{ZI} \end{bmatrix} \quad \begin{bmatrix} s_I^{(4)} \\ q_I^{(4)} \\ r_I^{(4)} \end{bmatrix} = [\mathbf{R}_4] \begin{bmatrix} X_I \\ Y_I \\ Z_I \end{bmatrix} \tag{18}$$

Expressions are similar for nodes J, M, L.θ_4 is the derivative of the displacement component w relatively to q_4. $\theta_4 = w_{,q4}$.

In the face IJLM, w is interpolated by ξ and η, the natural coordinates in the quadrangle IJML (ξ and η ∈[-1, 1]:

$$w = \frac{1}{4}(1-\xi)(1-\eta)w_i^{(4)} + \frac{1}{4}(1+\xi)(1-\eta)w_j^{(4)} + \frac{1}{4}(1+\xi)(1+\eta)w_m^{(4)} + \frac{1}{4}(1-\xi)(1+\eta)w_l^{(4)} \tag{19}$$

The derivatives of w with respect to ξ and η at node 4 are related to the nodal displacements:

$$\begin{Bmatrix} w_{,\xi} \\ w_{,\eta} \end{Bmatrix}_{(0,0)} = \frac{1}{4}\begin{bmatrix} -1 & 1 & 1 & -1 \\ -1 & -1 & 1 & 1 \end{bmatrix} \begin{bmatrix} w_i^{(4)} \\ w_j^{(4)} \\ w_m^{(4)} \\ w_l^{(4)} \end{bmatrix}, \quad \text{additionally} \quad \begin{Bmatrix} w_{,\xi} \\ w_{,\eta} \end{Bmatrix}_{(0,0)} = [\mathbf{J}_0] \begin{Bmatrix} w_{,s_4} \\ w_{,q_4} \end{Bmatrix}_{(0,0)} \tag{20}$$

Consequently,

$$\theta_4 = w_{,q4} = \frac{1}{2A_4}\begin{bmatrix} s_L^{(4)} - s_J^{(4)} & s_I^{(4)} - s_M^{(4)} & s_J^{(4)} - s_L^{(4)} & s_M^{(4)} - s_I^{(4)} \end{bmatrix} \begin{bmatrix} w_i^{(4)} \\ w_j^{(4)} \\ w_m^{(4)} \\ w_l^{(4)} \end{bmatrix} \tag{21}$$

A_4 is the surface of the face IJML (considering coordinates r_4 null).

$$A_4 = \left(\left(s_m^{(4)} - s_i^{(4)}\right)\left(q_l^{(4)} - q_j^{(4)}\right) + \left(q_m^{(4)} - q_i^{(4)}\right)\left(s_j^{(4)} - s_l^{(4)}\right)\right)/2 \tag{22}$$

Noting $P_4 = \frac{s_L^{(4)} - s_J^{(4)}}{2A_4}$ and $Q_4 = \frac{s_I^{(4)} - s_M^{(4)}}{2A_4}$ and considering Eq. (18),

$$\theta_4 = P_4\begin{bmatrix} r_{4x} & r_{4y} & r_{4z} \end{bmatrix} \begin{bmatrix} U_{XI} \\ U_{YI} \\ U_{ZI} \end{bmatrix} + Q_4\begin{bmatrix} r_{4x} & r_{4y} & r_{4z} \end{bmatrix} \begin{bmatrix} U_{XJ} \\ U_{YJ} \\ U_{ZJ} \end{bmatrix} - Q_4\begin{bmatrix} r_{4x} & r_{4y} & r_{4z} \end{bmatrix} \begin{bmatrix} U_{XM} \\ U_{YM} \\ U_{ZM} \end{bmatrix} - P_4\begin{bmatrix} r_{4x} & r_{4y} & r_{4z} \end{bmatrix} \begin{bmatrix} U_{XL} \\ U_{YL} \\ U_{ZL} \end{bmatrix} \tag{23}$$

The procedure to express the rotation θ_4 of the DKT element as a function of the displacement degrees of freedom of the prism does not require the IJML face to be planar. Nevertheless IJML must be close enough of the plane quadrangle defined by $r_4 = 0$ for each node because it is the surface of this plane quadrangle which is used in the calculation of A_4.

The rotations θ_5, θ_6 are expressed in the same manner according to the nodal displacements of the prism which give the expression of DKT rotations as a function of prism nodal displacements:

$$\begin{bmatrix} \theta_4 \\ \theta_5 \\ \theta_6 \end{bmatrix} = [\mathbf{T}][\mathbf{U}_e] \tag{24}$$

The curvatures are interpolated in function of the nodal displacements of the prism.

$$[\boldsymbol{\chi}] = \left([\mathbf{B}_\theta][\mathbf{T}] + [\overline{\mathbf{B}}_w]\right)[\mathbf{U}_e] = [\overline{\mathbf{B}}_b][\mathbf{U}_e] \tag{25}$$

3.3. Membrane deformation

For shell analysis, the DKT6 element is usually associated with a CST membrane element (Constant Strain Triangle) [38]. The in-plane displacements at nodes 1,2,3 are the average of the displacements of the corresponding upper and lower nodes of the prism. The in-plane displacements $[\mathbf{u}_m]$ at nodes 1,2,3 are expressed in function of $[\mathbf{U}_e]$, the nodal displacements of the prism. The membrane strain are classically interpolated in function of the in-plane displacements of nodes 1,2,3 and consequently in function of $[\mathbf{U}_e]$.

$$[\boldsymbol{\varepsilon}_m] = [\mathbf{B}_m][\mathbf{u}_m] = [\overline{\mathbf{B}}_m][\mathbf{U}_e] \tag{26}$$

The bending and membrane interpolation matrices are constant. This membrane contribution gives a stiffness to membrane deformation modes (modes 1, 2, 3 Fig. 2).

3.4. Transverse shear stabilization

Taking into account the 6×3 dof of the prism and the rigidities brought by the DKT, the membrane and the pinch, there are two modes of deformation which are with zero energy (Fig. 5a and b). Section 4.10 shows a case where these modes develop. To prevent the development of these modes, despite the use of the DKT approach, transverse shear deformations are calculated from node displacements and internal stabilization forces are calculated. This approach does not require a stabilization parameter.

Transverse shear strain calculation is based on the approach presented in Ref. [40,44] for a three node Mindlin shell element is used. It is an assumed strain method [1,32]. So-called assumed strain methods are based on the a-priori assumption of an interpolation for strains, generally different from those derived from the displacement interpolation. At each vertex node i of the middle plane triangle (i = 1,2,3), two material vectors $\mathbf{f}_1^i, \mathbf{f}_2^i$ are defined from i to the two other vertex nodes (Fig. 5c). The material coordinates along the sides are defined such as $r_1^i = r_2^i = 0$ at node i, $r_1^i = 1$ at node i+1 and $r_2^i = 1$ at node i-1. $\mathbf{f}_1^i$ and $\mathbf{f}_2^i$ are obtained from r_1^i and r_2^i:

$$\mathbf{f}_1^i = \frac{\partial \mathbf{x}}{\partial r_1^i}, \qquad \mathbf{f}_2^i = \frac{\partial \mathbf{x}}{\partial r_1^i} \qquad \mathbf{f}_3^i = \frac{\partial \mathbf{x}}{\partial \zeta} \tag{27}$$

The corresponding contravariant frame is such as:

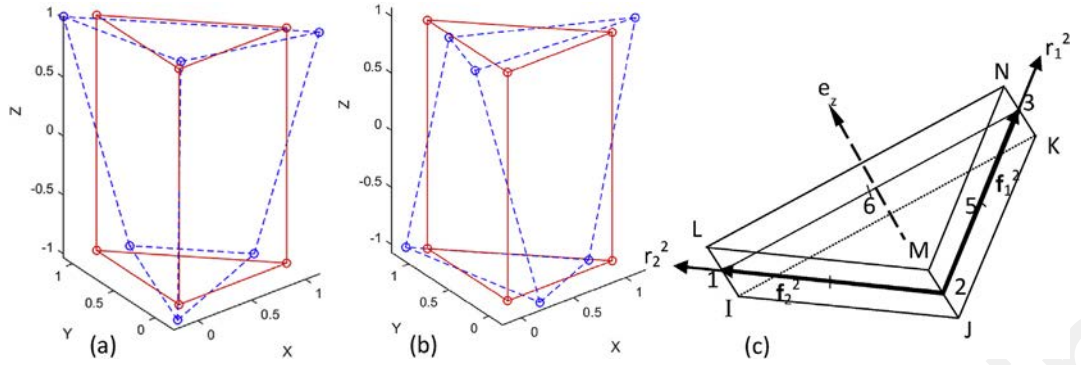

Fig. 5. (a) and (b) zero energy modes, (c) material coordinates and material vectors at node 2.

$$\mathbf{f}^i.\mathbf{f}_j = \delta^i_j \tag{28}$$

In the frame of the element sides, the components of the deformation tensor are denoted:

$$\boldsymbol{\varepsilon} = \widetilde{\varepsilon}_{kl}\,\mathbf{f}^k \otimes \mathbf{f}^l \tag{29}$$

The transverse shear $\widetilde{\varepsilon}_{\alpha 3} = \frac{1}{2}\,(\mathbf{f}_\alpha.\mathbf{f}_3 - \mathbf{f}_{\alpha 0}.\mathbf{f}_{30})$ ($\alpha = 1,2$) are assumed to be constant along each side and equal to the value at the center of the face of the prime.

Taking into account $\mathbf{f}^i_\alpha = \frac{\partial \mathbf{x}}{\partial r^i_\alpha} = \frac{\partial(\mathbf{x}_0+\mathbf{u})}{\partial r^i_\alpha} = \mathbf{f}^i_{\alpha 0} + \frac{\partial(\mathbf{u})}{\partial r^i_\alpha}$,

$$\widetilde{\varepsilon}^i_{\alpha 3} = \frac{1}{2}\left[\left(\frac{\partial \mathbf{u}}{\partial \zeta}\right)_m \cdot \left(\mathbf{f}^i_{\alpha 0}\right)_m + \left(\frac{\partial \mathbf{u}}{\partial r^i_\alpha}\right)_m \cdot \left(\mathbf{f}_{30}\right)_m\right] \tag{30}$$

At mid-point m ($m = 4, 5, 6$, Fig. 5c),

$$\left(\frac{\partial \mathbf{u}}{\partial \zeta}\right)_m = \frac{\mathbf{u}^B - \mathbf{u}^A}{2} \qquad \left(\frac{\partial \mathbf{u}}{\partial r^i_\alpha}\right)_m = \mathbf{u}^{i+1} - \mathbf{u}^i \tag{31}$$

A and B are nodes on the top and bottom surfaces on the normal at point i. Their displacement is the average of those of the corresponding vertex nodes. Eqs. (30) and (31) expresses the transverse shear strains $\widetilde{\varepsilon}^i_{\alpha 3}$ in function of the nodal displacements:

$$\left[\widetilde{\varepsilon}^i_{\alpha 3}\right] = [\mathbf{C}^i][\mathbf{U}_e] \tag{32}$$

The transverse shear strain components $\widetilde{\varepsilon}^i_{kl}$ at the three nodes i are expressed in the frame at node 1 (components ε^i_{mn}):

$$\widetilde{\varepsilon}^i_{kl}\,\mathbf{f}^{ki} \otimes \mathbf{f}^{li} = \varepsilon^i_{mn}\,\mathbf{f}^{m1} \otimes \mathbf{f}^{n1} \tag{33}$$

The vectors $\mathbf{f}^i_1$ and $\mathbf{f}^i_2$ are in the same plane which implies:

$$\begin{bmatrix}\varepsilon^i_{13}\\ \varepsilon^i_{23}\end{bmatrix} = [\mathbf{D}^i]\begin{bmatrix}\widetilde{\varepsilon}^i_{13}\\ \widetilde{\varepsilon}^i_{23}\end{bmatrix} \tag{34}$$

The transverse shear strains in the element are interpolated from these nodal transverse shears

$$\begin{bmatrix}\varepsilon_{13}\\ \varepsilon_{23}\end{bmatrix} = \sum_{i=1}^{3} \mathrm{N}^i(\xi,\eta)\begin{bmatrix}\varepsilon^i_{13}\\ \varepsilon^i_{23}\end{bmatrix} \tag{35}$$

In the present element, the transverse shear strains are assumed to be constant and equal to the value in the center of the element ($\xi = \eta = 1/3$).

Eq. (30)–(35) give the transverse shear interpolation matrix:

$$\begin{bmatrix}\varepsilon_{13}\\ \varepsilon_{23}\end{bmatrix} = \frac{1}{3}\sum_{1}^{3}[\mathbf{D}^i][\mathbf{C}^i][\mathbf{U}_e] = [\mathbf{B}_s][\mathbf{U}_e] \tag{36}$$

3.5. Through the thickness strain

3.5.1. Six node element

The through the thickness strain is an important capability of solid-shell elements that allows to analyze phenomena related to the thickness change. This section concerns the 'pinch modes' 4, 5, 6 (Fig. 2). By noting $h_1 = \eta\zeta$ and $h_2 = \xi\zeta$, the normal displacement in the direction $\mathbf{e}_z$ (Fig. 4) can be written:

$$w = a_{0w} + a_{xw}x + a_{yw}y + a_{zw}z + c_{1w}h_1 + c_{2w}h_2 \tag{37}$$

$$\text{with} \quad a_{xw} = [\mathbf{b}_x]^{\mathrm{T}}[\mathbf{U}_{ze}] \quad a_{yw} = [\mathbf{b}_y]^{\mathrm{T}}[\mathbf{U}_{ze}] \quad a_{zw} = [\mathbf{b}_z]^{\mathrm{T}}[\mathbf{U}_{ze}] \quad c_{\alpha w} = [\boldsymbol{\gamma}_\alpha]^{\mathrm{T}}[\mathbf{U}_{ze}] \quad (\alpha = 1,2) \tag{38}$$

$$[\boldsymbol{\gamma}_\alpha]^{\mathrm{T}} = \frac{1}{2}\left([\mathbf{h}_\alpha]^{\mathrm{T}} - \left([\mathbf{h}_\alpha]^{\mathrm{T}}[\mathbf{x}_e]\right)[\mathbf{b}_x]^{\mathrm{T}} - \left([\mathbf{h}_\alpha]^{\mathrm{T}}[\mathbf{y}_e]\right)[\mathbf{b}_y]^{\mathrm{T}} - \left([\mathbf{h}_\alpha]^{\mathrm{T}}[\mathbf{z}_e]\right)[\mathbf{b}_z]^{\mathrm{T}}\right) \tag{39}$$

$[\mathbf{h}_\alpha]^{\mathrm{T}}$ are the row matrix of the values of h_α at the six nodes.

$$[\mathbf{h}_1]^{\mathrm{T}} = [0 \quad 0 \quad -1 \quad 0 \quad 0 \quad 1] \quad [\mathbf{h}_1]^{\mathrm{T}} = [0 \quad -1 \quad 0 \quad 0 \quad 1 \quad 0] \tag{40}$$

$$\begin{bmatrix}[\mathbf{b}_x]^{\mathrm{T}}\\ [\mathbf{b}_y]^{\mathrm{T}}\\ [\mathbf{b}_z]^{\mathrm{T}}\end{bmatrix} = \left[\mathbf{J}_0^{-1}\right]\begin{bmatrix}[\mathbf{N}_{,\xi}]^{\mathrm{T}}\\ [\mathbf{N}_{,\eta}]^{\mathrm{T}}\\ [\mathbf{N}_{,\zeta}]^{\mathrm{T}}\end{bmatrix} \quad [\mathbf{J}_0] = \begin{bmatrix}[\mathbf{N}_{,\xi}]^{\mathrm{T}}\\ [\mathbf{N}_{,\eta}]^{\mathrm{T}}\\ [\mathbf{N}_{,\zeta}]^{\mathrm{T}}\end{bmatrix}[\mathbf{X}_e, \mathbf{Y}_e, \mathbf{Z}_e] \tag{41}$$

$[\mathbf{N}]^{\mathrm{T}}$ is the matrix of the interpolation functions of the prism.

$$[\mathbf{N}] = \frac{1}{2}[(1-\xi-\eta)(1-\zeta) \quad \xi(1-\zeta) \quad \eta(1-\zeta) \quad (1-\xi-\eta)(1+\zeta) \quad \xi(1+\zeta) \quad \eta(1+\zeta)] \tag{42}$$

Using the notation $a_{,x} = \frac{\partial a}{\partial x}$

$$w_{,z} = \left[[\mathbf{b}_z]^T + [\boldsymbol{\gamma}_1]^T h_{1,z} + [\boldsymbol{\gamma}_2]^T h_{2,z}\right][\mathbf{U}_{ze}] = \varepsilon^0_{zz} + q_{zz} \tag{43}$$

Where ε^0_{zz} is constant.

$$\varepsilon^0_{zz} = \frac{2}{h}\frac{1}{6}[-1 \quad -1 \quad -1 \quad 1 \quad 1 \quad 1][\mathbf{U}_{ze}] = [\mathbf{B}^p_0][\mathbf{U}_{ze}] \tag{44}$$

$$q_{zz} = \overline{J}_{33}\left[[\boldsymbol{\gamma}_1]^T\eta + [\boldsymbol{\gamma}_2]^T\xi\right][\mathbf{U}_{ze}] \tag{45}$$

A reduced integration consists in considering only the term ε_{zz}^0 in Eq. (43). q_{zz} enables to stabilize the zero energy modes due to the reduce integration [41]:

$$q_{zz} = [\mathbf{B}_\Gamma][\mathbf{U}_{ze}] \tag{46}$$

By noting Cp a stabilization coefficient, the through the thickness internal nodal loads are:

$$[\mathbf{F}_{\text{int}}^p] = \int_{V^e}\left([\mathbf{B}_0^p]^T + C^p[\mathbf{B}_\Gamma]^T\right)\ \sigma_{33}dV \tag{47}$$

If a 3D mechanical behavior is used, an element based on the above equations is subjected to thickness locking. This difficulty is caused by Poisson's ratio coupling of the in plane and transverse normal stress responses. When the element is in a pure bending state the through the thickness stress should be equal to zero. However the bending terms lead to a spurious normal stress when z is different from zero. This locking phenomenon can be overcome by uncoupling bending and through the thickness strains by a modification of the three-dimensional behavior law.

However, this approach can lead to difficulties in case of nonlinear material [25]. Different approaches have been proposed to overcome thickness locking. A method is proposed below that aims on the one hand to keep the complete 3D constitutive law and on the other hand to have a linear distribution of the normal stress and consequently to be able to verify stress boundary conditions on the top and bottom size of the prism.

3.5.2. Supplementary degree of freedom

An additional degree of freedom in the z direction is placed in the center G of the element (Fig. 6). Consequently the normal strain and stress are linear through the thickness (instead of constant without this dof). All the formulation presented above for different strains remain unchanged except the normal strain through the thickness ε_{zz}. The normal displacement along the central normal at $\xi = \eta = 0$ is quadratic in z.

$$w(z) = w(0) + \left(\frac{2z^2}{h^2} - \frac{z}{h}\right)w^- - \frac{4z^2}{h^2}w_o + \left(\frac{2z^2}{h^2} + \frac{z}{h}\right)w^+ \tag{48}$$

where w_o is the additional degree of freedom. w^- and w^+ are given from the displacements at the apex nodes. $w^+ = \frac{1}{3}(w_L + w_M + w_N)$ and $w^- = \frac{1}{3}(w_I + w_J + w_K)$.

Derivation of the normal displacement (Eq. (48)), gives the normal strain through the thickness:

$$\varepsilon_{zz} = \frac{1}{h}\left(w^+ - w^-\right) + \frac{4z}{h^2}\left(w^+ + w^- - 2w_o\right) = \frac{1}{h}\left(w^+ - w^- - 4\zeta w_o^*\right) \tag{49}$$

where $w_o^* = w_o - \frac{1}{2}(w^+ + w^-)$ is the "relative" translation dof.

The interpolation matrix $\mathbf{B}_{(1x19)}^p$ is obtained by adding one term (depending on ζ) given by Eq. (49) to the $\mathbf{B}_{(1x18)}^p$ of Eq. (44).

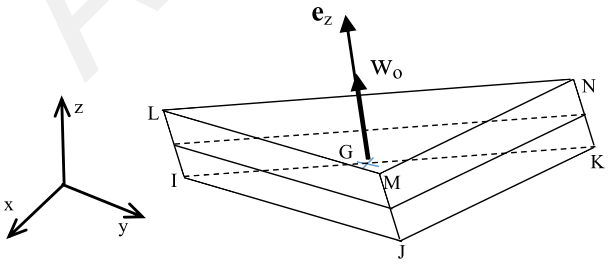

Fig. 6. Additional degree of freedom in the e_z direction at the center of the element.

The interest of this supplementary dof is double. The linear distribution of ε_{zz} avoids the thickness locking and the fully 3D constitutive law can be used. In addition, the pressure boundary conditions can be verified on the top and bottom surfaces of the prism, even in the case where the two pressures are different. This is important for the simulation of processes for which the distribution of the normal stress in the thickness is essential. This verification of the boundary conditions will be shown on some examples (while it is not verified for other solid shell elements.).

4. Numerical examples

The set of examples below aims to present the results obtained by the proposed prismatic solid-shell element to the classical tests for shell elements [45–47]. The proposed solid shell element is denoted SB7γ19 (section 3.5.2 and Fig. 6). It has 6 vertex nodes, 1 central node and 19 dof. The tests are also carried out with the prism element without central node and uncoupled constitutive matrix (SB6γ18). The results obtained by the proposed triangular prism solid-shell element are compared to the reference solution of the tests and to the solutions given by other finite elements. In particular, they are compared to the six node prism element SC6R used in Abaqus code [48]. This element is a solid shell with three translations degree of freedom per node.

In addition to these classical shell tests, the stress/strain through the thickness is analyzed in three tests: the circular clamped plate (section 4.3), the Scordelis-Lo roof the case of pressure loads on both sides (section 4.9) and the double dome forming (section 4.14).

4.1. Basic bending test

A square plate (lengths = 100 mm, thickness = 1 mm) is considered (Fig. 7) with three corners (1,6,8) simply supported. A point load is applied to the fourth one. The proposed SB7γ19 and SB6γ18 give the exact solution as the SCR6 (Abaqus) element (Table 1).

4.2. Patch test

The patch test is defined for triangular shell elements in Ref. [49,50] (Fig. 8). A theoretical constant state of bending moments all over the plate is given by the boundary conditions and concentrated loads

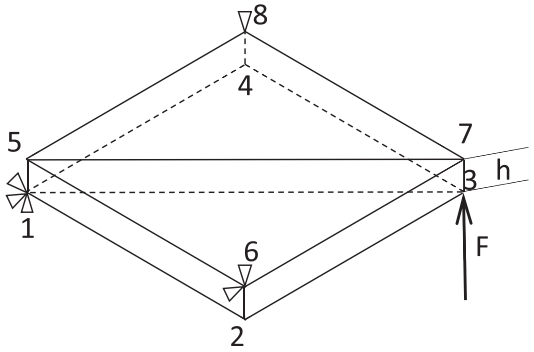

Fig. 7. Bending test.

Table 1
Comparison of bending test with different elements.

	SB6γ18	SB7γ19	SC6R (Abaqus)	C3D8 (Abaqus)	Ref
U_{z3}	0.39	0.39	0.3889	0.2230	0.39
$\sigma_{xx} = \sigma_{yy}$	0	0	2.10–4	wrong	0
σ_{xy}(top)	−3	−3	−2.993		−3
σ_{xy}(bottom)	3	3	2.986		3

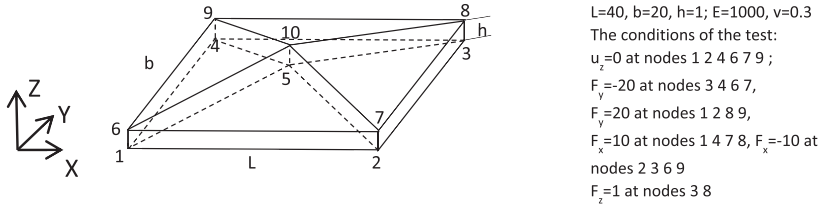

Fig. 8. Patch test.

Table 2
Patch test: Displacements at nodes.

	SB6γ18	SB7γ19	SC6R (Abaqus)	Ref
$w_3 = w_8$	−12,48	−12,48	−12,5334	−12,48
$w_5 = w_{10}$	−1,62	−1,62	−1,62896	−1,62

(Fig. 4b). Exact displacements at points 3, 5, 8 and 10 are obtained by the SB6γ18, SB7γ19 and SCR6 (Abaqus) elements (Table 2).

4.3. Circular clamped plate

A circular plate, the boundary of which is clamped, is subjected to a normal pressure. The useful data are: radius R = 100 mm; thickness = 1 mm; isotropic material: E = 200000 MPa, Poisson's ratio $\nu = 0.3$; uniform pressure normal to the bottom plane $p = 0.01172\ N/mm^2$. This value corresponds to a theoretical displacement of the plate center of 1 mm according to Kirchhoff's theory. Two densities of mesh have been considered (Fig. 9). The central displacement and normal stress are given in Table 3. The calculated displacement at plate center is accurate for the developed prism and also for the other shell elements considered. The dof at the center of the element (SB7γ19) leads to an exact normal stress component σ_{zz} that ranges from 0 to $0.01172\ N/mm^2$ and consequently verify the pressure boundary conditions. This not the case for the other elements.

A second pressure loading is considered to confirm the advantage of the developed solid-shell element with regard to the normal stress component σ_{zz}. A pressure P+ = -0.5*0.01172 is applied on the top surface, and a pressure P- = 1.5*0.01172 is applied on the bottom surface. The Table 4 confirms that the proposed prism (SB7γ19) leads to the exact normal stress that varies through the thickness from P- to P+. It is not the case of the other elements. The Scordelis-Lo roof with pressure test (presented in section 4.9) analyses the normal stress in a curved geometry.

Table 3
Center displacement and stress component normal to the mid-plane.

Coarse mesh	SB6γ18	SB7γ19	SC6R (Abaqus)	DKT18 [35]	Ref
Uc	0,924083	0,924083	0,86347	1,1	1
σ_{zz} top	−0,00586058	0	0	0	0
σ_{zz} bottom	−0,00586058	−0,01172	0	0	−0,01172
Refined mesh					
Uc	1,0044	0,995576	0.99339	1.027	1
σ_{zz} top	−0,00586982	0	0	0	0
σ_{zz} bottom	−0,00586982	−0,01172	0	0	−0.01172

Table 4
Center displacement and stress component when a pressure P+ = -0.5*0.01172 is applied on the top surface, and a pressure P- = 1.5*0.01172 is applied on the bottom surface.

Coarse mesh	SB6γ18	SB7γ19	SC6R (Abaqus)	Ref
Uc top	0.84288	0.92427	0.88854	1
Uc bottom	0.84288	0.92427	0.88854	1
σ_{zz} top	−0,01172	−0,01172*0.5	0	−0,01172*0.5
σ_{zz} bottom	−0,01172	−0,01172*1.5	0	−0,01172*0.5
Refined mesh				
Uc top	0.98818	0.99580	0.99339	1
Uc bottom	0.98818	0.99580	0.99339	1
σ_{zz} top	−0,01172	−0,01172*0.5	0	−0,01172*0.5
σ_{zz} bottom	−0,01172	−0,01172*1.5	0	−0,01172*0.5

4.4. Twisted beam

The 90°-twisted beam intend to assess the effect of warping on the performance of shell elements. The undeformed beam twisted by 90°

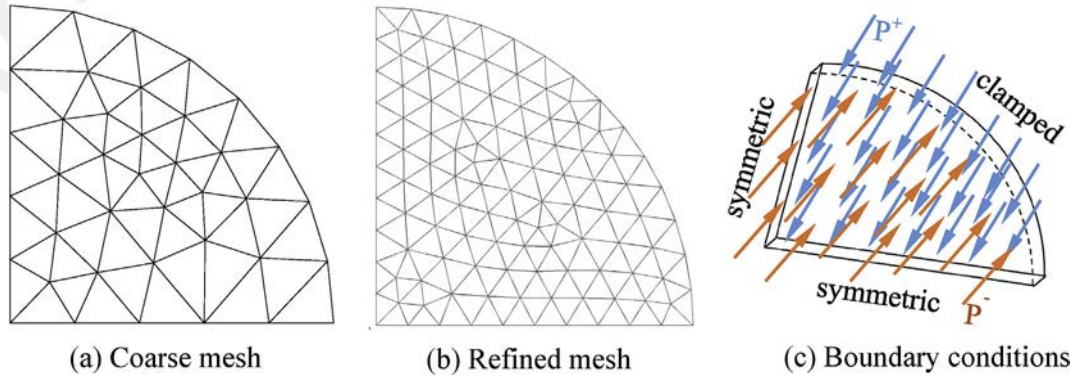

Fig. 9. Clamped circular plate (an only quarter due to symmetries) subjected to a pressure.

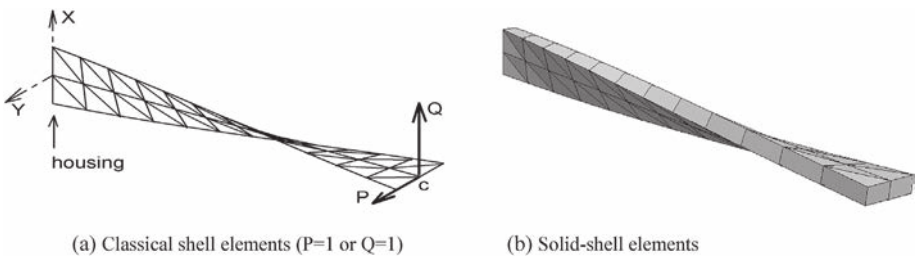

(a) Classical shell elements (P=1 or Q=1) (b) Solid-shell elements

Fig. 10. Twisted beam.

Table 5
Twisted beam: Loading point displacement.

'In-plane "P"	SB6γ18	SB7γ19	SC6R (Abaqus)	DKT18	Morley [43]	S3 [51]	Ref
Mesh 12 × 2	0,99269912	0,99252581	0,99419248	0,9821	0,993	0,9749	1
Mesh 48 × 8	0,99529867	0,99524336	0,99693953	0,9935	0,995	0988	1
Out-of-plane "Q"							
Mesh 12 × 2	0,8422691	0,84082098	1,05292474	0,8352	0,8449	0,8312	1
Mesh 48 × 8	0,97696693	0,97605473	0,99149943	0,9743	0,9755	0,9709	1

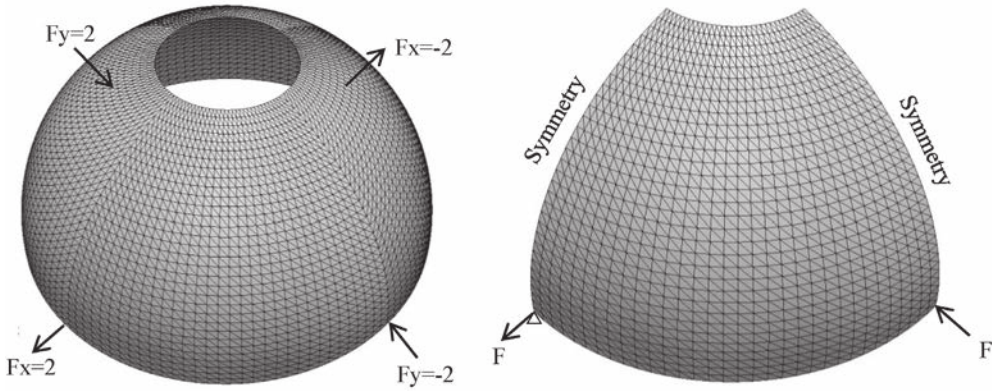

(a) Complete structure (b) 32x32 mesh (quarter)

Fig. 11. Pinched hemispherical shell.

with a 12 by 2 mesh is shown in Fig. 10. The length of the beam is 12.0, width 1.1, thickness 0.32, elasticity modulus 2.9×10^7 Pa, Poisson ratio 0.22. If an "in-plane" force P (P = 1) is applied on the point C along Y direction (Fig. 4a), the resulting displacement UY(C) = 5.424×10^{-3}. If an "out-of-plane" force Q (Q = 1) is prescribed along X, the theoretical displacement UX(C) = 1.754×10^{-3}.

The results relating to a 12 by 2 mesh (Table 5) and a 48 by 8 mesh of different triangular shell elements and the solid shell elements are given in Table 5. The comparison of numerical values to exact solutions show that the proposed prism is not prone to warping even if prismatic

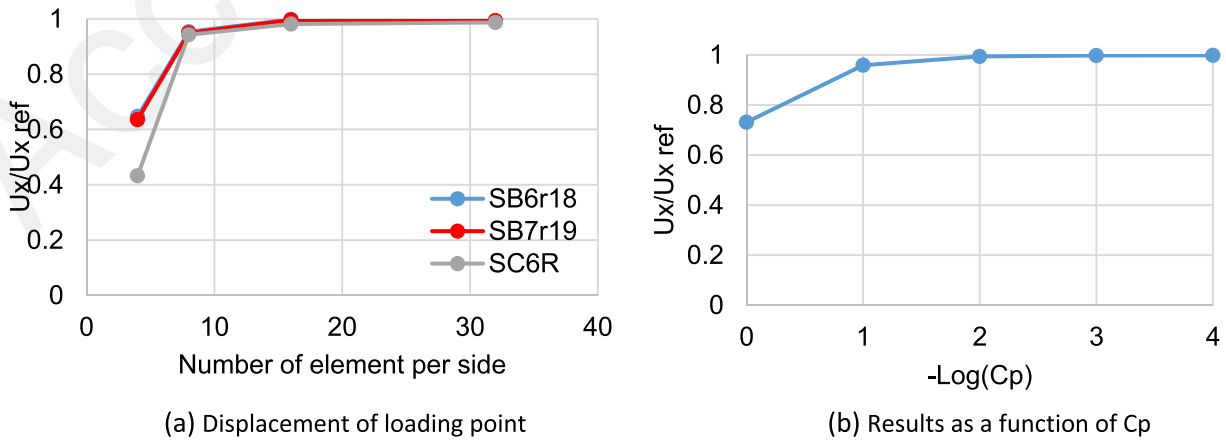

(a) Displacement of loading point (b) Results as a function of Cp

Fig. 12. Convergence of the displacement for the pinched hemisphere.

Table 6
Pinched hemispherical shell: Loading point displacement for different elements.

	SB6γ18	SB7γ19	SC6R (Abaqus)	DKT18 [38]	Morley [43]	S3 [51]	Ref
Mesh 4 × 4	0,060870	0,059780	0,040690	0,09804	0,10961	0,08196	0,093/0094
Mesh 8 × 8	0,089640	0,089238	0,088650	0,09463	0,1	0,08367	
Mesh 16 × 16	0,093820	0,093665	0,092260	0,09296	0,09522	0,08652	

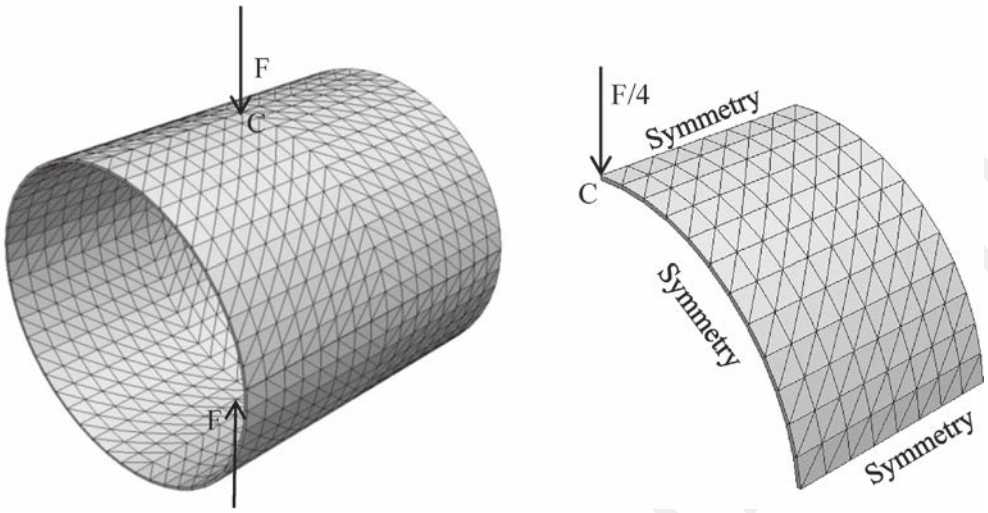

Fig. 13. Pinched cylinder with free ends.

Table 7
Pinched cylinder: Loading point displacement for different type of elements.

	SB6γ18	SB7γ19	SC6R (Abaqus)	DKT18 [38]	Morley [43]	S3 [51]
Mesh 4 × 4	0,97827919	0,975505	0,897278	0,504	1176	1043
Mesh 6 × 6	0,99736611	1,027752	0,945250	0,751	1092	1017
Mesh 8 × 8	1,03338016	1,032792	0,965189	0,875	1062	1,01

elements require a fine mesh on this test.

4.5. Pinched hemisphere with 18° hole

A hemispherical thin shell (radius R = 10, thickness h = 0.04), with an 18° circular cutout at its pole, is subjected to an inward force (Fy = −2) and to an outward force (Fx = 2) (Fig. 11). The material is isotropic elastic with Young's modulus $E = 6.825 \times 10^7$ Pa and Poisson's ratio v = 0.3. Owing to symmetry, one-quarter of the shell is modeled (Fig. 11). The loading points displacements are compared to the reference result given in Ref. [45]: Ux = - Uy = 0.093 It can be noted that other authors propose another reference value: 0.094 [35]

For three meshes (4 × 4), (8 × 8), (16 × 16), the displacements under the loads are compared with the reference in Table 6. The proposed prism gives good results.

4.6. Sensitivity to the pinch coefficient

The sensitivity to the pinch coefficient has been studied (Fig. 12). The curve in Fig (12b) shows the displacement of loading points relatively to the reference result as a function of the coefficient for pinching C_p (Eq. (47)), for a fixed 16 × 16 mesh. The curve shows satisfactory

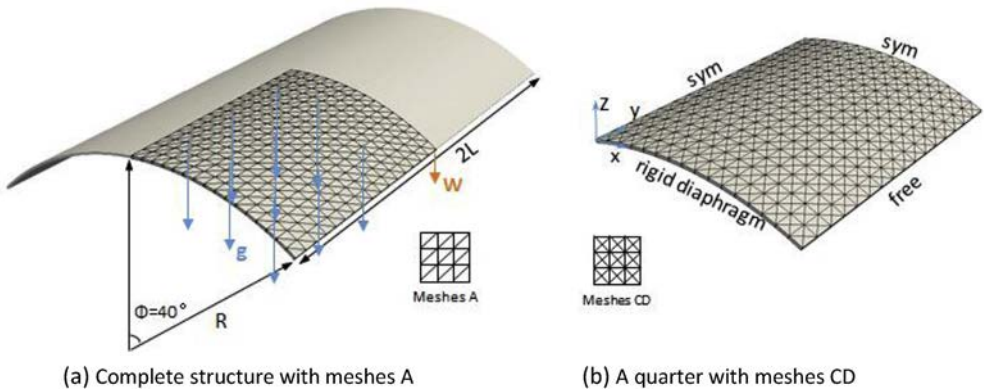

Fig. 14. Scordelis-Lo roof.

convergence when $C_p \leq 10^{-2}$. This analysis was done in all of the tests presented in this paper. Beyond the pinched hemisphere, none of them showed any sensitivity to the given value Cp. But all the calculations were also conducted with very low Cp values (10^{-4}) without showing hourglass problem.

4.7. Pinched cylinder with free ends

The pinched cylinder problem shown in Fig. 13 was also frequently analyzed to test shell elements. The useful data are: Cylinder: length $L = 10.35$, radius $R = 4.953$, thickness $h = 0.094$; Material: $E = 10.5 \times 10^7$ Pa and $\nu = 0.3125$; Load: Two equal and opposite forces $F = 100$. Due to symmetries, only an eighth of a pinched cylinder is meshed (Fig. 13). The vertical displacement of point C, which can be compared to the solution: 0.1139, in Table 7.

4.8. Scordelis-Lo roof

The geometry consists of a portion of a cylindrical shell (Fig. 14). Its two end sections are fixed using rigid diaphragms while its two lateral sides remain free. It is subjected to a distributed loading. Only one quarter of the structure needs to be modeled. The useful data are: length $L = 50$, radius $R = 25$, thickness $t = 0.25$, $\Phi = 40°$; Material: $E = 4.32 \times 10^7$ Pa and $\nu = 0.0$; Gravity Load: $g = 90$. The test result is the vertical displacement at the midpoint of the free edge. The theoretical value for this result is $u_{ref} = 0.3024$.

Fig. 15 presents the curves of the normalized displacement at the midpoint of the free edge with two different types of mesh: mesh A and cross-diagonal (CD) mesh (Fig. 14). The test is a membrane dominated problem. The proposed prism shows correct convergence compared to other elements.

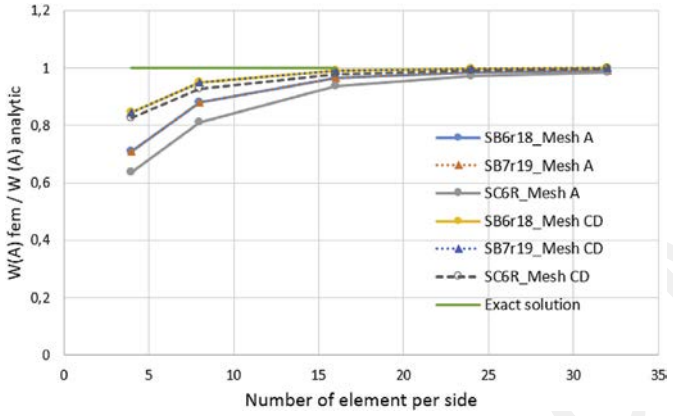

Fig. 15. Convergence of normalized deflection at free edge's mid-point w.

Table 8
Stress through the thickness in the Scordelis-Lo roof subjected to pressure.

σ_{zz} Bottom	SB6 γ18	SB7γ19	SC6R	Ref
Case 1: $P^- = 10$, $P^+ = 0$	−5	−10	0	−10
Case 2: $P^- = 10$, $P^+ = -10$	−10	−10	0	−10
Case 3: $P^- = 10$, $P^+ = -5$	−10	−10	0	−10
σ_{zz} Top	SB6 γ18	SB7γ19	SC6R	Ref
Case 1: $P^- = 10$, $P^+ = 0$	−5	0	0	0
Case 2: $P^- = 10$, $P^+ = -10$	−10	−10	0	−10
Case 3: $P^- = 10$, $P^+ = -5$	−5	−5	0	−5

4.9. Scordelis-Lo roof subjected to pressure

The Scodelis-Lo roof has been modified, with the same geometry and boundary conditions, except that the gravity load has been replaced by pressures applied normally to its two faces. Three pressure loadings with different values of P- and P+, on the bottom and top of the shell are considered. The mesh is a type A 24×24 elements. The results presented in Table 8 show that the proposed solid-shell element SB7γ19 is able to obtain the correct normal stress through the thickness in the case with curved plate. The normal stress distribution is shown in Fig. 16. The stress boundary conditions are well verified.

4.10. Stabilization of zero-energy modes

The square plate ($L = 100$, $e = 10$) is meshed by 8 prism elements and subjected to loads as shown Fig. 17a. Without stabilization (i.e. with the stiffness of the DKT, membrane and pinch but no transverse shear stiffness) a deformation is obtained as shown Fig. 17b and c. It corresponds to the development of the mode shown in Fig. 5a. Taking into account the transverse shear energy stabilizes this deformation mode (Fig. 17d).

4.11. Mesh with distorsion

A square plate ($L = 100$, $h = 1$) with different distorsions of the mesh is analyzed (Fig. 18).

The analysis of a simply supported square plate submitted to a constant pressure is made using meshes with distorsion. The vertices at the 3 nodes are not normal to the middle surface. The distorsion reduces the accuracy of the calculation. Nevertheless, the result remains rather close to the solution.

4.12. Cantilever beam with a point load

To assess the performance of the solid-shell elements in geometric nonlinear analysis, several shell benchmarks were carried out below. The first one is the cantilever beam subjected to a point load P ($P_{max} = 4$) at the free end (Fig. 19a). The geometry is $L = 10$, $b = 1$, $h = 0.1$. The material data is: Young's modulus $E = 1.2 \times 10^7$ Pa, Poisson's ratio $= 0$. Fig. 19b shows the calculated load-deflection curves obtained with a 16×1 mesh with the solid-shell elements SB6γ18, SB7γ19. They are

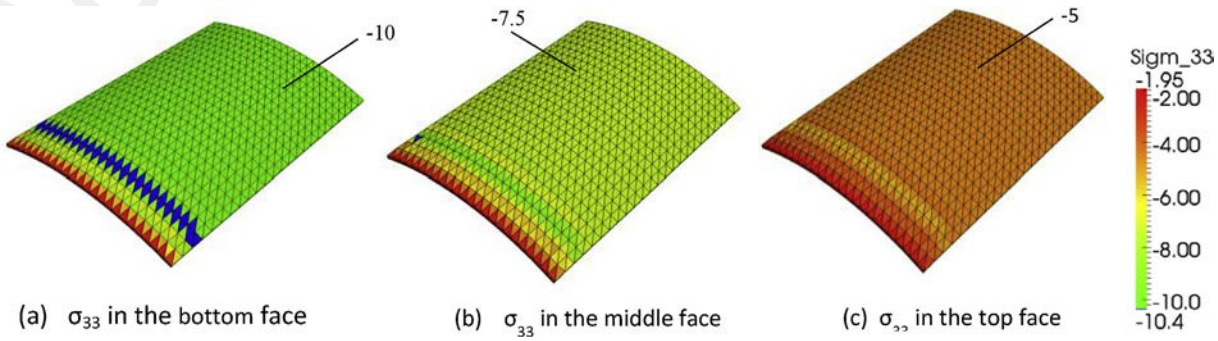

Fig. 16. Distribution of transverse stress σ_{33} in case 3 ($P^- = 10$, $P^+ = -5$).

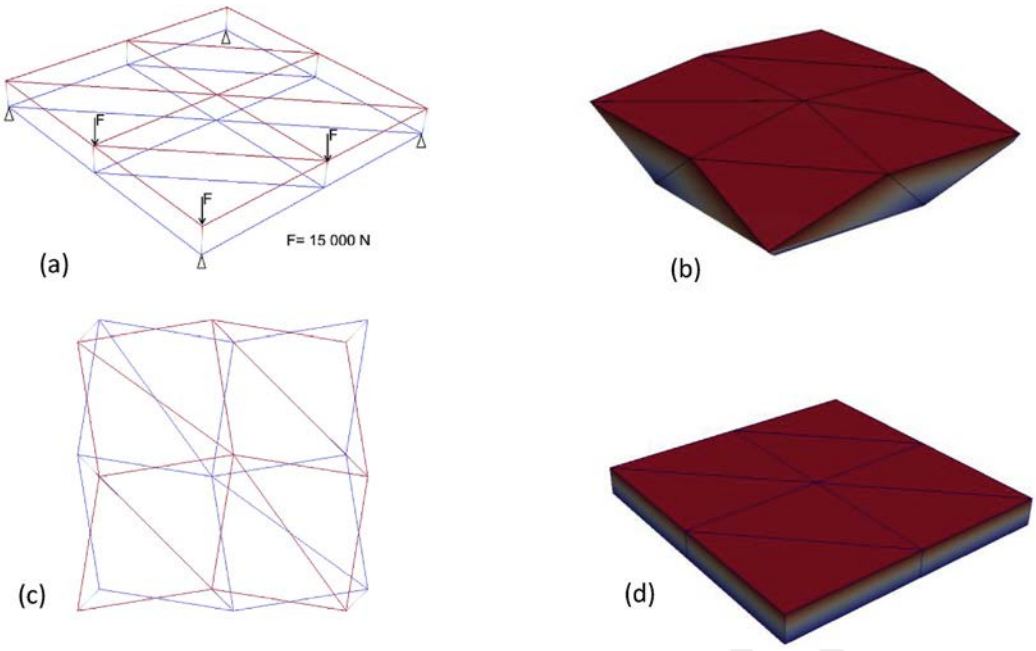

Fig. 17. Development of zero energy modes, (a) mesh and loading, (b) zero energy mode, (c) top view, (d) transverse shear stabilization.

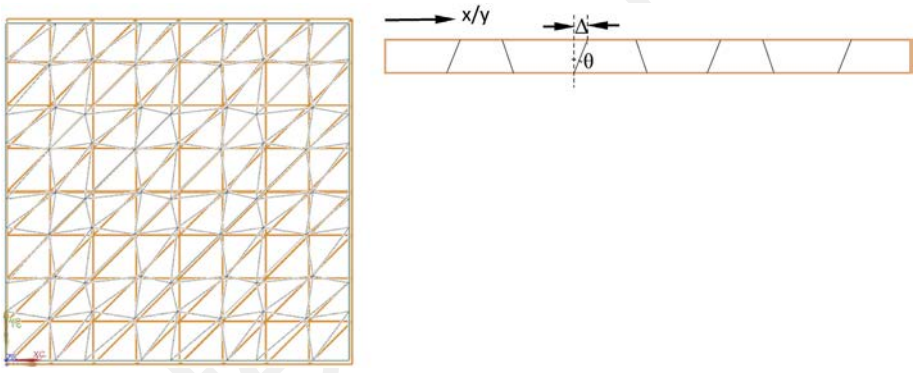

Fig. 18. Simply supported square plate wit distorted meshes.

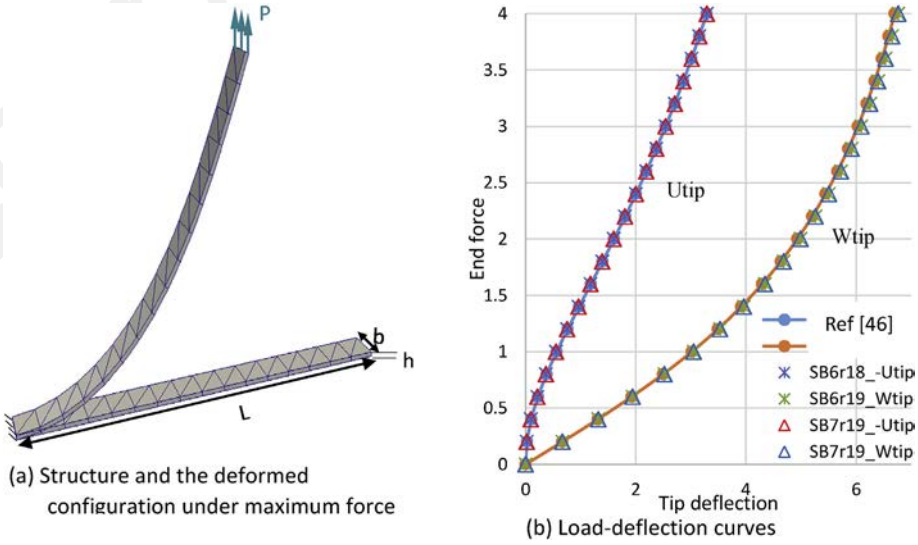

Fig. 19. Cantilever beam.

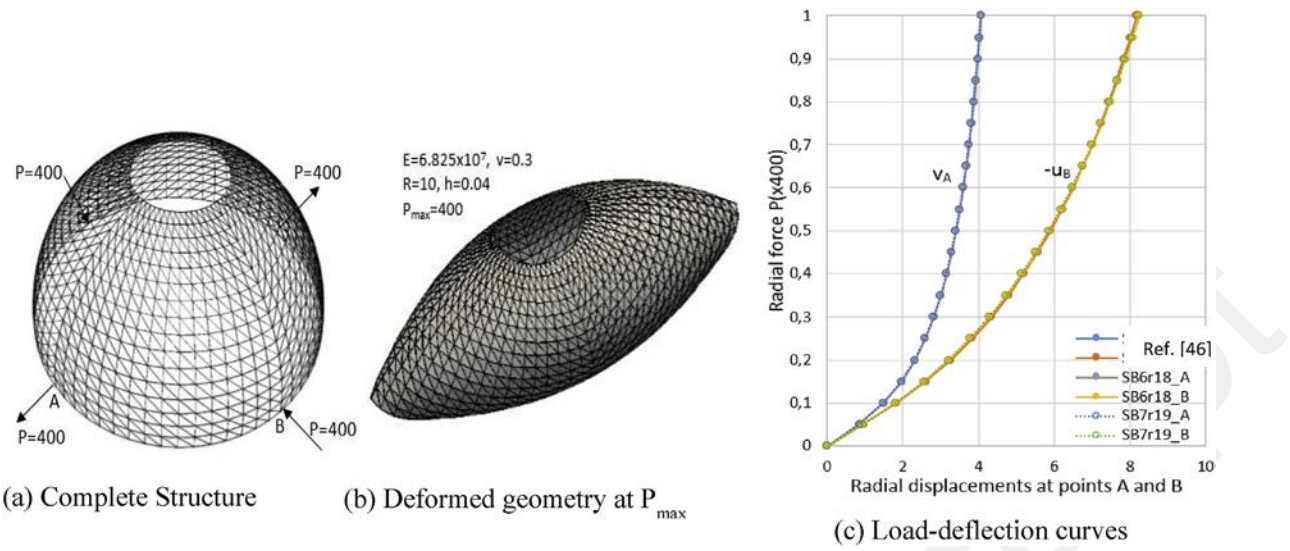

Fig. 20. Hemispherical shell subjected to alternating radial forces.

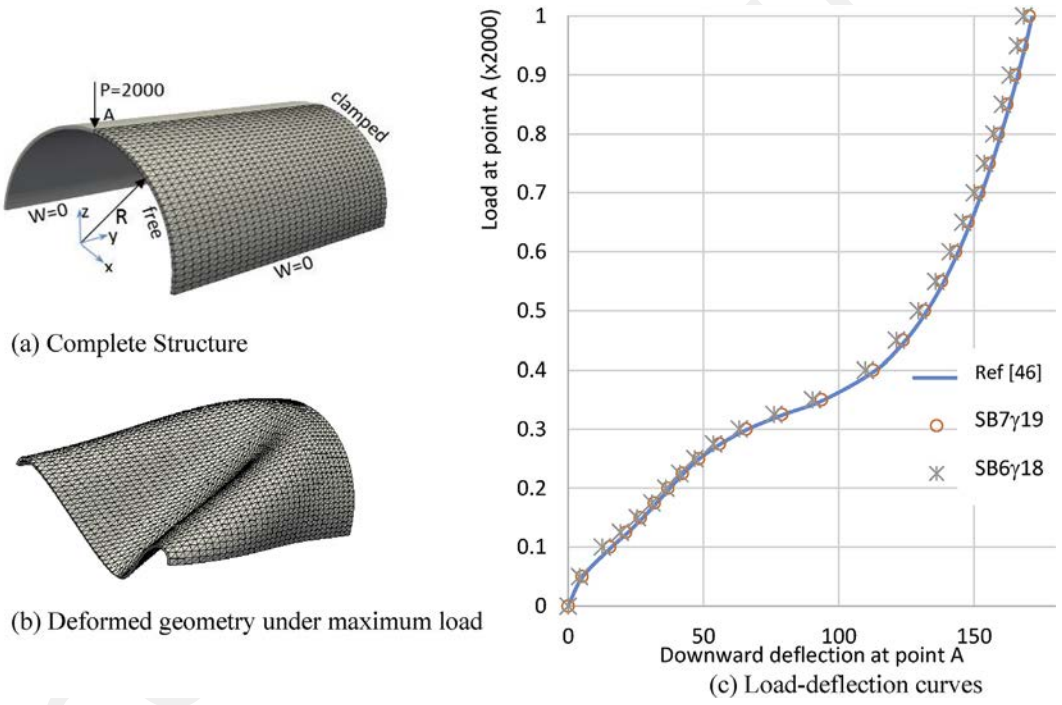

Fig. 21. Pinched semi-cylindrical isotropic shells subjected to a pinching force.

compared to the reference solution given in Ref. [46]. The proposed element shows good performance in the analysis of this test.

4.13. Hemispherical shell subjected to alternating radial forces

The pinched hemisphere shell problem in analyzed in the context of large elastic deformations (Fig. 20). Due to symmetry, only a quarter of the hemisphere is modelled by a 16×16 mesh. The material and geometric properties are given in section 4.4. The point load is incrementally applied to a maximum value Pmax = 400 N. Fig. 20b shows the deformed configuration obtained with the maximum load. The load-deflection curves at points A and B are plotted in Fig. 20c. The displacements obtained with the proposed SB7γ19 prism are in good agreement with the reference solution [46].

4.14. Pinched semi-cylindrical isotropic shell

This semi-cylindrical shell is subjected to a vertical radial force at the middle A of the free circumferential edge, while the other circumferential edge is fully clamped. Along the two straight edges, all the nodal Z translations are restrained. The material properties are E = 2068.5, v = 0.3. The length and radius of the half cylinder are L = 3.048 and R = 1.016, respectively, and the thickness is h = 0.03. The maximum load level at point A is set to Pmax = 2000. The structure is modeled using 32×32 element meshes of SB6γ18, SB7γ19 elements and compared to the reference [46]. Fig. 21b shows the deformed shape for the maximum load level, and Fig. 21c plots the obtained load-displacement at point A. The results obtained with the proposed element are in good agreement with the reference results.

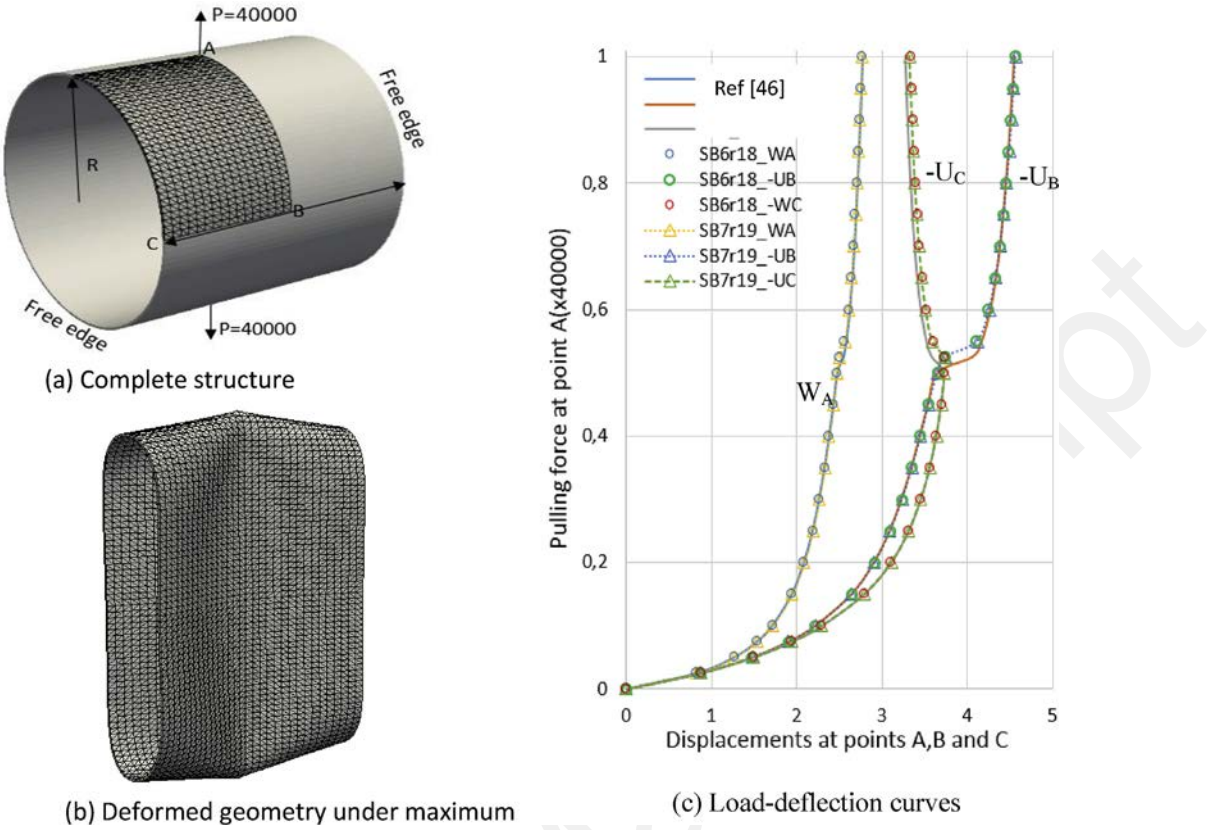

Fig. 22. Open-end cylindrical shell subjected to radial pulling forces.

4.15. Pullout of an open-ended cylindrical shell

An opened cylindrical shell is pulled by a pair of radial forces P (Fig. 22). The parameters are: length $L = 10.35$, radius $R = 4.953$, thickness $h = 0.094$, material properties: $E = 10.5 \times 10^7$, $v = 0.3125$. The maximum load is $Pmax = 4 \times 10^4$. Taking the advantage of the symmetry, only one octant of the cylinder is modelled and a 16×16 regular mesh is employed. Fig. 22b shows the deformed shell under the maximum load. In Fig. 22c the predicted displacements at points of loading are compared with the reference solution [46]. Close agreement can be noted. When P reaches 2×10^4, a slight snap-through behavior caused by buckling was found, that is fairly well obtained by the proposed element.

4.16. Consolidation in a double dome forming

The 'Double Dome Benchmark' is a relatively complex double-curve geometry (Fig. 23 for a quarter of the part). It has been defined for comparative studies between models and approaches in forming continuous dry and pre-impregnated reinforcements [52–57].

In the thermoforming of thermoplastic prepreg, it is important to consolidate the composite i.e. to remove the voids that appear when it is heated. For this a pressure is applied for a certain time at a given temperature. Fig. 1 shows a prepreg during forming (with about 10% void) and after consolidation (no visible voids). To produce a good quality composite, this phase is essential. The forming and the consolidation phase have been simulated using the SB7γ19 prismatic solid-shell proposed in the present work. It gives the through the thickness stress during forming and consolidation. From the stress state and the temperature applied during a time interval, the 'degree of intimate contact' can be calculated following the works of Lee and springer [16]. This 'degree of intimate contact' is equal to 1 when the prepreg is consolidated (no void). The simulation using the proposed prism provides the stress through the thickness at the end of the forming phase which makes it possible to calculate the degree of intimate contact (Fig. 23). In this state the consolidation of the prepreg is not is not reached. A 3-min consolidation

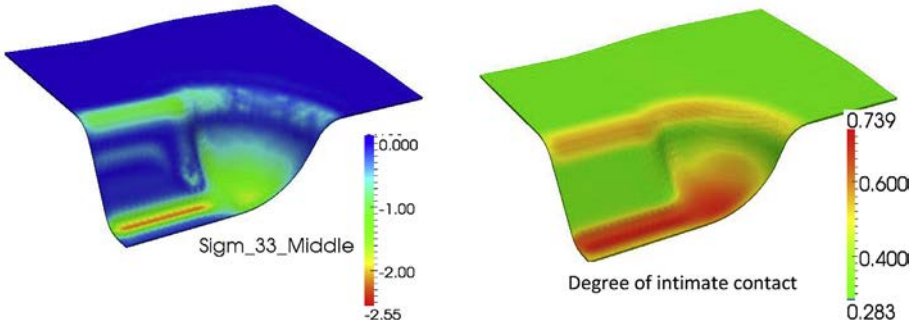

Fig. 23. Normal stress through the thickness and degree of intimate contact after forming.

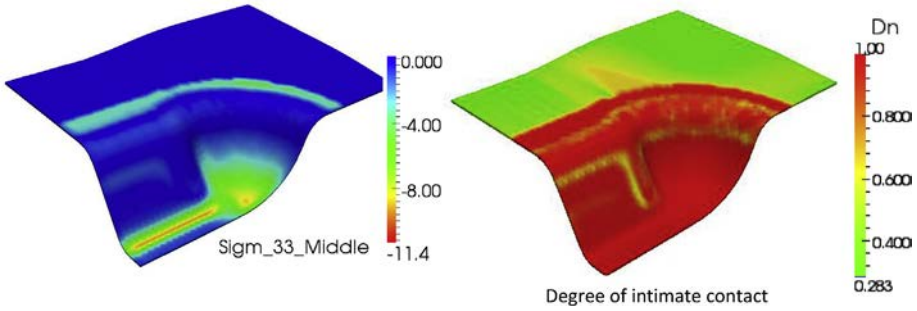

Fig. 24. Normal stress through the thickness and degree of intimate contact after consolidation.

phase leads to a degree of intimate contact equal to one on the whole double dome (Fig. 24). This is a typical use of the proposed prismatic solid shell element. It is efficient during the simulation of the forming stage and it provides the through the thickness stress that render possible the intimate contact calculation during the consolidation phase.

5. Conclusion

In this paper a prismatic solid-shell element has been proposed. The purpose of this element is sheet forming simulations especially when the through the thickness behavior is important. This is the case for prepreg thermoforming processes in which a consolidation stage compact the prepreg to remove voids. The proposed prismatic shell element is based on a DKT formulation that leads to a good efficiency on classical shell tests. The supplementary dof at the center of the element (a translation normal to the mid-surface) allows to use a 3D constitutive equation. Above all, it leads to a linear strain/stress in thickness and render possible to verify load boundary conditions on the top and bottom surface of the shell. This is important for simulation of sheet forming processes and in particular prepreg consolidation.

The use of solid-shell elements in composite forming simulations is not very common at present. However phenomena in the thickness are often critical during forming of these materials. The stiffness through the thickness of composite reinforcements or prepreg is often weak and the deformation can be important. The consolidation (Fig. 1) was mentioned in this paper. The compaction of textile preforms during infusion process due to atmospheric pressure on the bagging film modifies the thickness of the composite and is a sensitive point in the process. In these cases, the use of solid-shell finite elements must make it possible to simulate both the shaping of the reinforcements or prepreg and the deformations in the thickness.

Acknowledgements

This work was supported by the Agence de l'environnement et de la maitrise de l'energie (ADEME), as part of the project STIICPA.

References

[1] E.N. Dvorkin, K.J. Bathe, A continuum mechanics based four-node shell element for general non-linear analysis, Eng. Comput. 1 (1) (1984) 77–88.
[2] T. Belytschko, B.L. Wong, H. Stolarski, Assumed strain stabilization procedure for the 9-node Lagrange shell element, Int. J. Numer. Meth. Eng. 28 (2) (1989) 385–414.
[3] E. Onate, O.C. Zienkiewicz, B. Suarez, R.L. Taylor, A general methodology for deriving shear constrained Reissner-Mindlin plate elements, Int. J. Numer. Meth. Eng. 33 (2) (1992) 345–367.
[4] B. Brank, J. Korelc, A. Ibrahimbegović, Nonlinear shell problem formulation accounting for through-the-thickness stretching and its finite element implementation, Comput. Struct. 80 (9–10) (2002) 699–717.
[5] I. Katili, I.J. Maknun, J.L. Batoz, A. Ibrahimbegovic, Shear Deformable Shell Element DKMQ24 for Composite Structures. Composite Structures, On line, 2018.
[6] J.C. Simo, M.S. Rifai, A class of mixed assumed strain methods and the method of incompatible modes, Int. J. Numer. Meth. Eng. 29 (8) (1990) 1595–1638.
[7] U. Andelfinger, E. Ramm, EAS-elements for two-dimensional, three-dimensional, plate and shell structures and their equivalence to HR-elements, Int. J. Numer. Meth. Eng. 36 (8) (1993) 1311–1337.
[8] R.F. Valente, R.N. Jorge, R.P. Cardoso, J.C. de Sá, J.J. Grácio, On the use of an enhanced transverse shear strain shell element for problems involving large rotations, Comput. Mech. 30 (4) (2003) 286–296.
[9] J.L. Batoz, K.J. Bathe, L.W. Ho, A study of three-node triangular plate bending elements, Int. J. Numer. Meth. Eng. 15 (12) (1980) 1771–1812.
[10] J.L. Batoz, An explicit formulation for an efficient triangular plate-bending element, Int. J. Numer. Meth. Eng. 18 (7) (1982) 1077–1089.
[11] R. Ayad, G. Dhatt, J.L. Batoz, A new hybrid-mixed variational approach for Reissner–Mindlin plates: the MiSP model, Int. J. Numer. Meth. Eng. 42 (1998) 1149–1179.
[12] S. Klinkel, F. Gruttmann, W. Wagner, A robust non-linear solid shell element based on a mixed variational formulation, Comput. Meth. Appl. Mech. Eng. 195 (1–3) (2006) 179–201.
[13] F. Gruttmann, W. Wagner, A stabilized one-point integrated quadrilateral Reissner–Mindlin plate element, Int. J. Numer. Meth. Eng. 61 (13) (2004) 2273–2295.
[14] T. Belytschko, H. Stolarski, W.K. Liu, N. Carpenter, J.S. Ong, Stress projection for membrane and shear locking in shell finite elements, Comput. Meth. Appl. Mech. Eng. 51 (1–3) (1985) 221–258.
[15] T. Belytschko, B.L. Wong, H.Y. Chiang, Advances in one-point quadrature shell elements, Comput. Meth. Appl. Mech. Eng. 96 (1) (1992) 93–107.
[16] W.I. Lee, G.S. Springer, A model of the manufacturing process of thermoplastic matrix composites, J. Compos. Mater. 21 (11) (1987) 1017–1055.
[17] S.C. Mantell, G.S. Springer, Manufacturing process models for thermoplastic composites, J. Compos. Mater. 26 (16) (1992) 2348–2377.
[18] D. Soulat, A. Cheruet, P. Boisse, Simulation of continuous fibre reinforced thermoplastic forming using a shell finite element with transverse stress, Comput. Struct. 84 (13–14) (2006) 888–903.
[19] R. Hauptmann, K. Schweizerhof, A systematic development of 'solid-shell' element formulations for linear and non-linear analyses employing only displacement degrees of freedom, Int. J. Numer. Meth. Eng. 42 (1) (1998) 49–69.
[20] L. Vu-Quoc, X.G. Tan, Optimal solid shells for non-linear analyses of multilayer composites. I. Statics, Comput. Meth. Appl. Mech. Eng. 192 (9–10) (2003) 975–1016.
[21] S. Reese, A large deformation solid-shell concept based on reduced integration with hourglass stabilization, Int. J. Numer. Meth. Eng. 69 (8) (2007) 1671–1716.
[22] R.A. De Sousa, J.W. Yoon, R.P.R. Cardoso, R.F. Valente, J.J. Grácio, On the use of a reduced enhanced solid-shell (RESS) element for sheet forming simulations, Int. J. Plast. 23 (3) (2007) 490–515.
[23] F. Abed-Meraim, A. Combescure, An improved assumed strain solid–shell element formulation with physical stabilization for geometric non-linear applications and elastic–plastic stability analysis, Int. J. Numer. Meth. Eng. 80 (13) (2009) 1640–1686.
[24] M. Schwarze, S. Reese, A reduced integration solid-shell finite element based on the EAS and the ANS concept—large deformation problems, Int. J. Numer. Meth. Eng. 85 (3) (2011) 289–329.
[25] B. Bassa, F. Sabourin, M. Brunet, A new nine-node solid-shell finite element using complete 3D constitutive laws, Int. J. Numer. Meth. Eng. 92 (7) (2012) 589–636.
[26] F.G. Flores, A simple reduced integration hexahedral solid-shell element for large strains, Comput. Meth. Appl. Mech. Eng. 303 (2016) 260–287.
[27] K.Y. Sze, W.K. Chan, A six-node pentagonal assumed natural strain solid–shell element, Finite Elem. Anal. Des. 37 (8) (2001) 639–655.
[28] F.G. Flores, Development of a non-linear triangular prism solid-shell element using ANS and EAS techniques, Comput. Meth. Appl. Mech. Eng. 266 (2013) 81–97.
[29] Y. Ko, P.S. Lee, A 6-node triangular solid-shell element for linear and nonlinear analysis, Int. J. Numer. Meth. Eng. 111 (13) (2017) 1203–1230.
[30] K.Y. Sze, A. Ghali, Hybrid hexahedral element for solids, plates, shells and beams by selective scaling, Int. J. Numer. Meth. Eng. 36 (9) (1993) 1519–1540.
[31] T.H. Pian, P. Tong, Relations between incompatible displacement model and hybrid stress model, Int. J. Numer. Meth. Eng. 22 (1) (1986) 173–181.
[32] T.J. Hughes, T. Tezduyar, Finite elements based upon Mindlin plate theory with particular reference to the four-node bilinear isoparametric element, J. Appl. Mech. 48 (3) (1981) 587–596.

[33] J.C. Simo, D.D. Fox, M.S. Rifai, On a stress resultant geometrically exact shell model. Part III: computational aspects of the nonlinear theory, Comput. Meth. Appl. Mech. Eng. 79 (1) (1990) 21–70.
[34] N. Büchter, E. Ramm, D. Roehl, Three-dimensional extension of non-linear shell formulation based on the enhanced assumed strain concept, Int. J. Numer. Meth. Eng. 37 (15) (1994) 2551–2568.
[35] R.P. Cardoso, J.W. Yoon, M. Mahardika, S. Choudhry, R.J. Alves de Sousa, R.A. Fontes Valente, Enhanced assumed strain (EAS) and assumed natural strain (ANS) methods for one-point quadrature solid-shell elements, Int. J. Numer. Meth. Eng. 75 (2) (2008) 156–187.
[36] K.Y. Sze, L.Q. Yao, A hybrid stress ANS solid-shell element and its generalization for smart structure modelling. Part I—solid-shell element formulation, Int. J. Numer. Meth. Eng. 48 (4) (2000) 545–564.
[37] A.B. Bettaieb, J.V. de Sena, R.A. de Sousa, R.A.F. Valente, A.M. Habraken, L. Duchêne, On the comparison of two solid-shell formulations based on in-plane reduced and full integration schemes in linear and non-linear applications, Finite Elem. Anal. Des. 107 (2015) 44–59.
[38] J.L. Batoz, G. Dhatt, Modélisation des structures par éléments finis, vol. 3, Coques, Hermès, 1992.
[39] E. Oñate, F. Zarate, F. Flores, A simple triangular element for thick and thin plate and shell analysis, Int. J. Numer. Meth. Eng. 37 (15) (1994) 2569–2582.
[40] P. Boisse, J.L. Daniel, J.C. Gelin, A C0 three-node shell element for non-linear structural analysis, Int. J. Numer. Meth. Eng. 37 (14) (1994) 2339–2364.
[41] T. Belytschko, W.K. Liu, B. Moran, Nonlinear Finite Elements for Continua and Structures, John Wiley & Sons Inc., 2000.
[42] Y.Q. Guo, J.L. Batoz, H. Naceur, S. Bouabdallah, F. Mercier, O. Barlet, Recent developments on the analysis and optimum design of sheet metal forming parts using a simplified inverse approach, Comput. Struct. 78 (1) (2000) 133–148.
[43] L.S.D. Morley, The constant-moment plate-bending element, J. Strain Anal. 6 (1) (1971) 20–24.
[44] P. Boisse, J.C. Gelin, J.L. Daniel, Computation of thin structures at large strains and large rotations using a simple C0 isoparametric three-node shell element, Comput. Struct. 58 (2) (1996) 249–261.
[45] H. Macneal, L. Harder, A proposed standard set of problems to test finite element accuracy, Finite Elem. Anal. Des. 1 (1985) 3–20.
[46] K.Y. Sze, X.H. Liu, S.H. Lo, Popular benchmark problems for geometric nonlinear analysis of shells, Finite Elem. Anal. Des. 40 (11) (2004) 1551–1569.
[47] K.J. Bathe, A. Iosilevich, D. Chapelle, An evaluation of the MITC shell elements, Comput. Struct. 75 (1) (2000) 1–30.
[48] Abaqus Analysis User's Guide, Dassault Systèmes Simulia Corp., Providence, RI, USA.
[49] J. Robinson, Element evaluation. A set of assessment points and standard tests, Proc. FEM Commerc. Environ. 1 (1978) 217–248.
[50] J.L. Batoz, An explicit formulation for an efficient triangular plate-bending element, Int. J. Numer. Meth. Eng. 18 (7) (1982) 1077–1089.
[51] F. Sabourin, M. Brunet, Detailed formulation of the rotation-free triangular element "S3" for general purpose shell analysis, Eng. Comput. 23 (5) (2006) 469–502.
[52] A. Willems, S.V. Lomov, I. Verpoest, D. Vandepitte, P. Harrison, W.R. Yu, Forming simulation of a thermoplastic commingled woven textile on a double dome, Int. J. Material Form. 1 (1) (2008) 965–968.
[53] W. Lee, M.K. Um, J.H. Byun, P. Boisse, J. Cao, Numerical study on thermo-stamping of woven fabric composites based on double-dome stretch forming, Int. J. Material Form. 3 (2) (2010) 1217–1227.
[54] M.A. Khan, T. Mabrouki, E. Vidal-Sallé, P. Boisse, Numerical and experimental analyses of woven composite reinforcement forming using a hypoelastic behaviour. Application to the double dome benchmark, J. Mater. Process. Technol. 210 (2) (2010) 378–388.
[55] J. Sargent, J. Chen, J. Sherwood, J. Cao, P. Boisse, K. Vanclooster Willem, S.V. Lomov, M. Khan, T. Mabrouki, K. Fetfatsidis, D. Jauffrès, Benchmark study of finite element models for simulating the thermostamping of woven-fabric reinforced composites, Int. J. Material Form. 3 (1) (2010) 683–686.
[56] X. Peng, Z.U. Rehman, Textile composite double dome stamping simulation using a non-orthogonal constitutive model, Compos. Sci. Technol. 71 (8) (2011) 1075–1081, 86.
[57] P. Harrison, R. Gomes, N. Curado-Correia, Press forming a 0/90 cross-ply advanced thermoplastic composite using the double-dome benchmark geometry, Compos. Appl. Sci. Manuf. 54 (2013) 56–69.